Biosensors and Bioelectronics 258 (2024) 116318

Contents lists available at ScienceDirect

Biosensors and Bioelectronics

journal homepage: www.elsevier.com/locate/bios

Massive field-of-view sub-cellular traction force videography enabled by Single-Pixel Optical Tracers (SPOT)

Xing Haw Marvin Tan [a,b,g], Yijie Wang [e], Xiongfeng Zhu [a], Felipe Nanni Mendes [a], Pei-Shan Chung [a,b], Yu Ting Chow [a], Tianxing Man [a], Hsin Lan [a], Yen-Ju Lin [c], Xiang Zhang [a], Xiaohe Zhang [d], Thang Nguyen [b], Reza Ardehali [e], Michael A. Teitell [b,f], Arjun Deb [e], Pei-Yu Chiou [a,b,*]

[a] Department of Mechanical and Aerospace Engineering, University of California Los Angeles, Westwood Plaza, Los Angeles, CA, 90095, United States
[b] Department of Bioengineering, University of California Los Angeles, Westwood Plaza, Los Angeles, CA, 90095, United States
[c] Department of Electrical and Computer Engineering, University of California at Los Angeles, Westwood Plaza, Los Angeles, CA, 90095, United States
[d] Department of Mathematics, University of California Los Angeles, 520 Portola Plaza, Los Angeles, CA, 90095, United States
[e] Division of Cardiology, Department of Medicine, David Geffen School of Medicine, University of California Los Angeles, 675 Charles E Young Dr S, Los Angeles, CA, 90095, United States
[f] Department of Pathology and Laboratory Medicine, David Geffen School of Medicine, University of California Los Angeles, 675 Charles E Young Dr S, Los Angeles, CA, 90095, United States
[g] Department of Electronics and Photonics, Institute of High Performance Computing (IHPC), Agency for Science, Technology and Research (A*STAR), 1 Fusionopolis Way, 138632, Singapore

ARTICLE INFO

Keywords:
Diffraction grating
Cell traction force
Bio-MEMS

ABSTRACT

We report a massive field-of-view and high-speed videography platform for measuring the sub-cellular traction forces of more than 10,000 biological cells over 13 mm^2 at 83 frames per second. Our Single-Pixel Optical Tracers (SPOT) tool uses 2-dimensional diffraction gratings embedded into a soft substrate to convert cells' mechanical traction force into optical colors detectable by a video camera. The platform measures the sub-cellular traction forces of diverse cell types, including tightly connected tissue sheets and near isolated cells. We used this platform to explore the mechanical wave propagation in a tightly connected sheet of Neonatal Rat Ventricular Myocytes (NRVMs) and discovered that the activation time of some tissue regions are heterogeneous from the overall spiral wave behavior of the cardiac wave.

1. Introduction

Mechanical forces regulate biological processes at scales spanning across molecules (Bao et al., 2010), cells (Zancla et al., 2022), tissues (Biggs et al., 2020; Ladoux and Mège, 2017), organs (Pocaterra et al., 2019), and up to enabling the survival and growth of multicellular organisms by facilitating, for example, heart beating (Matonia et al., 2020), blood vessel contraction (James and Allen, 2018), intestinal food digestion (Sensoy, 2021), and body movements (Dasbiswas et al., 2018). These multicellular activities require the coordination of complex combinations of electrical, chemical, and mechanical processes (Ellefsen et al., 2019). Tools and techniques for analyzing multicellular systems are readily available in the electrical (Dean et al., 2008), and chemical domains (Cameron et al., 2016), but approaches for assessing multiscale mechanical processes are currently lacking and inferred. This technology gap is especially evident for rapid and dynamically coordinated events that can involve the collective interactions of many cells over large distances (Cansız et al., 2018).

Current approaches used to quantify the mechanical properties of cells and tissues include atomic force microscopy (AFM) (Cross et al., 2007; Rodriguez et al., 2013), traction force microscopy (TFM) (Sabass et al., 2008), elastic pillars (EPs) (Fu et al., 2010; Xiao et al., 2018), muscular thin films (MTF) (Grosberg et al., 2011), and fluorescently labeled elastomeric contractible surfaces (FLECS) (Pushkarsky et al., 2018). A comparison of these technologies is listed in Table 1. AFM provides high spatial resolution and high sensitivity measurements but

* Corresponding author. Department of Mechanical and Aerospace Engineering, University of California Los Angeles, Westwood Plaza, Los Angeles, CA, 90095, United States.
E-mail address: peiyu@g.ucla.edu (P.-Y. Chiou).

https://doi.org/10.1016/j.bios.2024.116318
Received 7 February 2024; Received in revised form 15 April 2024; Accepted 17 April 2024
Available online 24 April 2024

depends on probe tip placement and has low throughput (Hardij et al., 2013). TFM quantifies traction forces by tracking the movement of nanoparticles embedded in an elastic substrate (Sabass et al., 2008; Vorselen et al., 2020; Yokota et al., 2020). EPs extract cellular traction forces by measuring the bending of elastic micropillars (Saez et al., 2010). Both TFM and EP methods require high numerical aperture (N.A.) optics to determine nanoparticle or micropillar movements for accurate measurements. The small field-of-view (FOV) of high N.A. optics, however, limits the number of cells for concurrent assessments, which is the major hurdle for studying interconnected multicellular systems that change dynamically during short time periods. Measurement accuracy and reproducibility may be adversely affected when data from numerous cells in a large area is generated by assembling sequential readings taken from smaller regions within a more extensive process, particularly when the conditions of the cells change during the measurement period. Elastomer post (Yokota et al., 2020) and MTF approaches measure the average force output of a group of cells based on the deformation of a pillar or a film. These force averaging methods lack information of individual cells, subgroups of cells, and their synergistic or antagonistic effects. FLECS can provide high throughput single cell measurements, although this approach requires seeding isolated cells on tracer structures, thereby preventing FLECS from quantifying interconnected multicellular systems.

Current measurements of mechanical wave propagation in tissues

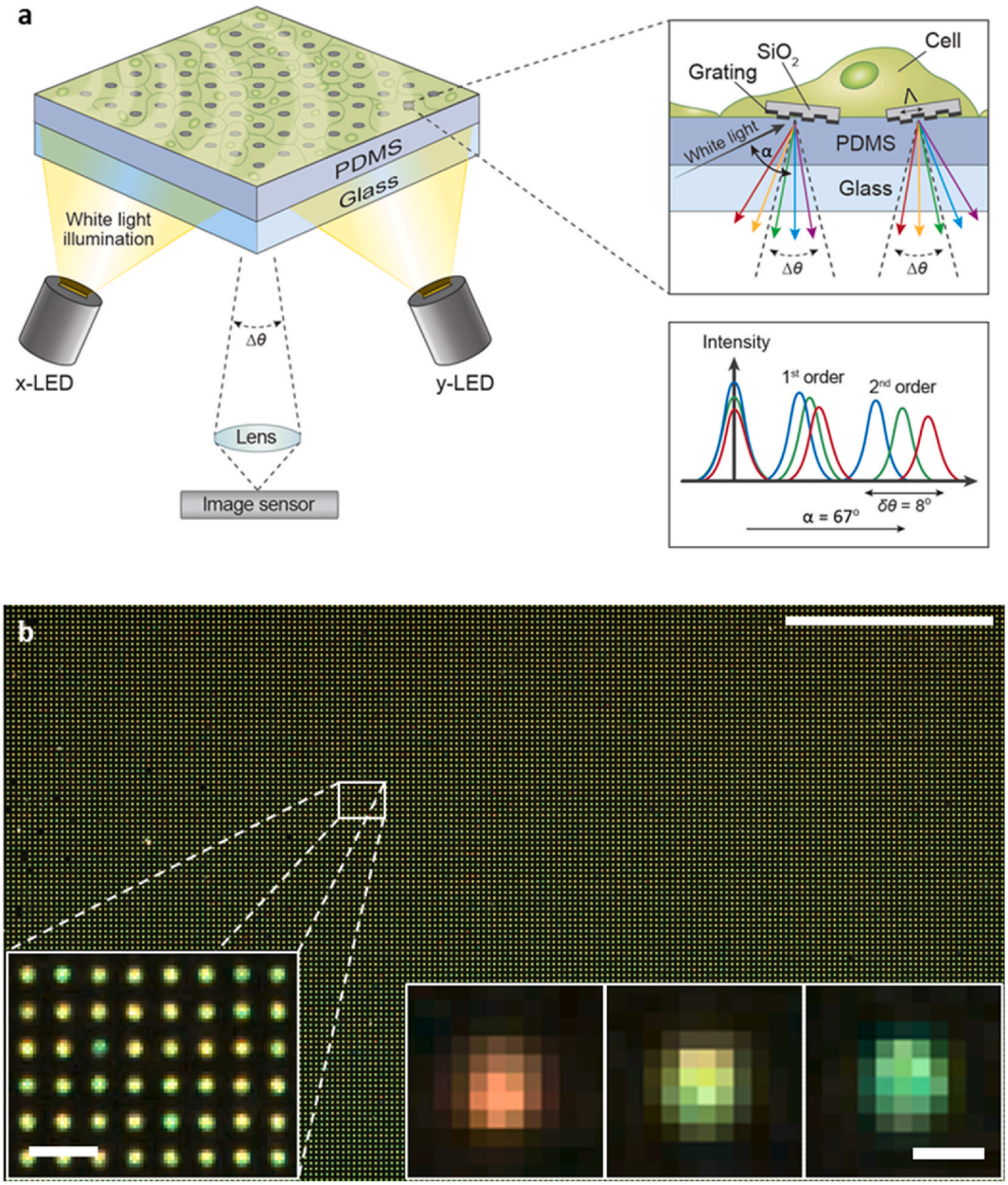

Fig. 1. SPOT microscopy for quantitative measurements of mechanical wave propagation in two-dimensional interconnected tissues. a, SPOT microscopy consists of an array of diffraction grating micromirrors bonded on top of an elastic PDMS sheet. Cells exert traction force on the substrate and cause the micromirrors to tilt. Each grating micromirror reflects and disperses incident white light into microscale rainbow light rays. Second-order diffraction maxima are chosen for their optimal dynamic range and sensitivity in measurements. A low N.A. lens is used to collect a narrow color band from the rainbow light rays of each micromirror for imaging. When a micromirror is tilted, the collected color band changes according to the extent of tilting. **b**, A representative image captured by SPOT microscopy. The bottom right inset shows the micromirror images that represent tilting angles of −4, 0, and +4°, respectively. The field-of-view spans 4.82 mm by 2.71 mm, and the videos were taken at a frame rate of 83 frames per second. (Scale bars: top right, 1 mm; bottom left, 50 μm; bottom right, 10 μm).

use optical mapping (OM) methods (Kappadan et al., 2020; Lapp et al., 2017; McPheeters et al., 2017; Tsukamoto et al., 2016). However, OM has several fundamental limitations. Firstly, OM requires cell labeling with fluorescing dyes, such as Di-8-ANEPPS or Fluo-4 AM. Compromised cell viability can occur with OM because of the photochemical toxicity related to high concentration dye and intense illumination for high-speed fluorescence imaging over extended imaging times, while probe quenching can limit periods of data collection. Secondly, OM is an indirect force measurement method. It relies upon cells' electrical or chemical signals to indicate cells' mechanical responses. The relationship between these indirect indicators and mechanical activity and strength are inconsistent and vary amongst cells (Kappadan et al., 2020; Lapp et al., 2017; McPheeters et al., 2017; Tsukamoto et al., 2016). Furthermore, fluorescent detection does not provide information on force direction, which is a crucial parameter for constructing traction force distribution. As a result, it is not possible to extract traction force data using traditional OM methods.

Here, we introduce an innovative concept and approach called Single-Pixel Optical Tracers (SPOT) microscopy. SPOT microscopy directly measures rapid coordinated or asynchronous changes in traction forces of cells within a large interconnected multicellular sheet with sub-cellular resolution (Table 1 in the Supplementary Materials). This approach overcomes major limitations of conventional OM because there are no fluorescing labels, thus eliminating photochemical toxicity and probe quenching over extended imaging times. SPOT microscopy is also a direct force measurement method. Color change of light is useful in many different applications ranging from photocatalysis degradation (Al-Nayili and Alhaidry, 2023) to colorimetric interferometry (Zhu et al., 2021). Color changes recorded on SPOT images emerge from the tilting of grated micromirrors actuated by the applied traction forces from the overlying cells (Fig. 1a). This feature removes the uncertainty of indirect mechanical response measurements inferred from conventional electrical and chemical signaling methods.

2. Experimental section

SPOT microscopy requires a platform of periodic, arrayed micromirrors that harbor micro-fabricated reflective optical gratings (Figs. 1a and 2). The design of each disk is circular (Figs. 1a and 2d). The linewidths and spacings of the diffraction grating are 600 nm (Supplementary Fig. S5). The disks are made from thermally grown silicon dioxide (SiO_2). The thickness of each disk is 1560 nm. The geometry of the SiO_2 disk on top of the polydimethylsiloxane (PDMS) substrate are shown in Supplementary Figs. S4a and b. The reflective diffraction gratings are made from a stack of $Ti/Al/Ti/SiO_2$ as illustrated in Supplementary Fig. S5. Under broadband light illumination, each micromirror grating separates the light into its constituent frequencies, reflecting a rainbow of colored light rays. When overlying cells apply directional force on the micromirror-containing substrate, a micromirror tilts, which tilts the reflected color rainbow. Since the position of the illuminating light does not change, the tilting of the micromirrors causes different wavelengths of light to enter the lens of the camera. Due to the small numerical aperture (N.A.) of the camera's lens , only a narrow spectrum of wavelengths gets imaged by the camera. This results in different colors detected by the camera for different tilting angles of the micromirrors. A low N.A. Canon MP-E 65 mm f/2.8 optical lens collects the reflected light rays from the micromirror array onto an image sensor (see Supplementary Methods). The low N.A. lens functions as a bandpass color filter to permit the collection of a narrow, reflected color band ($\Delta\theta$) from each micromirror in a large imaging field. When a specific micromirror in the imaging field tilts, its reflected band shifts, causing a color change on the image sensor (Fig. 1b).

Quantitative measurement of traction force requires data that includes the force direction, which demands a measurement of micromirror tilting angles in both the x and y directions. The detection of x direction tilting ang y direction tilting of micromirrors are sequentially recorded at two time frames separated by 12 msec on a high speed camera through controlled LEDs illumination in the x and y directions. The experimental details are provided in Section 1 of the Supplementary Methods and Supplementary Fig. S6. To extract the tilting angles of each micromirror, we performed Gaussian intensity fitting on imaging pixels for each micromirror in each of the three color channels (R, G, B). Since there are two directions, x and y, the tilting angle of each micromirror is encoded using six color values, three for the x-direction and three for the y-direction. After obtaining the RGB values for each micromirror, we convert the RGB color scheme into the hue-saturation-value (HSV) color scheme because the Hue value is an ideal parameter for quantifying the color band reflected by a micromirror as it represents the dominant wavelength of a color. A machine learning approach using B-spline regression (PyEarth) was employed to fit the multi-dimensional models (Fig. 3a and b) to the experimental data (Fig. 3c and d). The curve fitting errors for the tilting angles in the x and y directions are plotted as histograms (Fig. 3e and f). The median errors for the tilting angles in the x and y directions are 0.21 deg and 0.16 deg, respectively. Our current iteration of the SPOT microscopy can measure tilting angle changes between -4 to $+4^\circ$ in both x and y directions (Fig. 3a–d).

To extract the traction force distribution of Neonatal Rat Ventricular Myocytes (NRVMs) from measured micromirror tilting angles using SPOT microscopy, we applied a machine learning method to train on 2000 simulated examples of tilting angles generated by the finite element method (FEM) using COMSOL Multiphysics. Each simulated example maps a 2D random traction force distribution to a tilting angle distribution of a 5×5 micromirror array (see Supplementary Methods Section 6). With the information of tilting angles in the x and y directions for each micromirror on SPOT, we can use the trained machine learning model to calculate the 2D traction force distribution of these cells

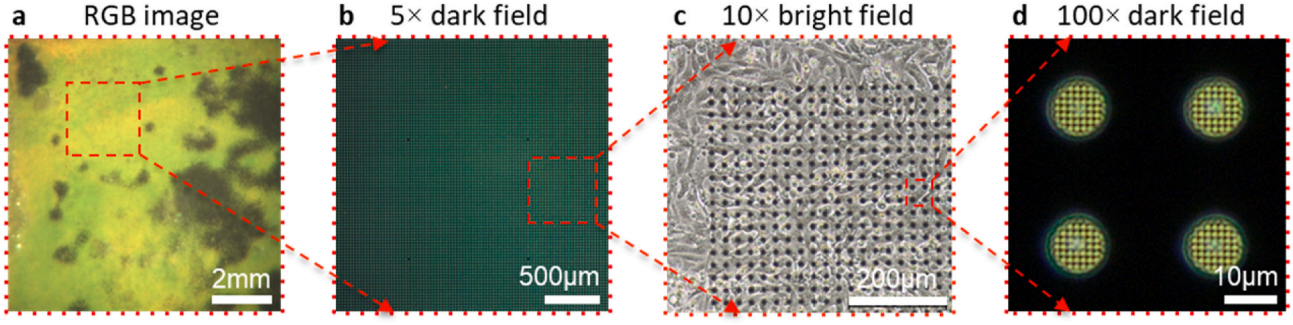

Fig. 2. Comparison of SPOT microscopy images with microscopic images of different magnifications. **a**, An image captured by the SPOT microscopy. The field-of-view spans 9 mm by 9 mm, and the videos were taken at a frame rate of 44 frames per second. **b**, A 5 × dark field image showing an array of micromirrors on the SPOT platform. **c**, A 10 × bright field image showing the relative size of micromirrors and a sheet of NRVMs cultured on a SPOT platform. **d**, A 100 × dark field image showing the 2D optical grating pattern on individual micromirrors..

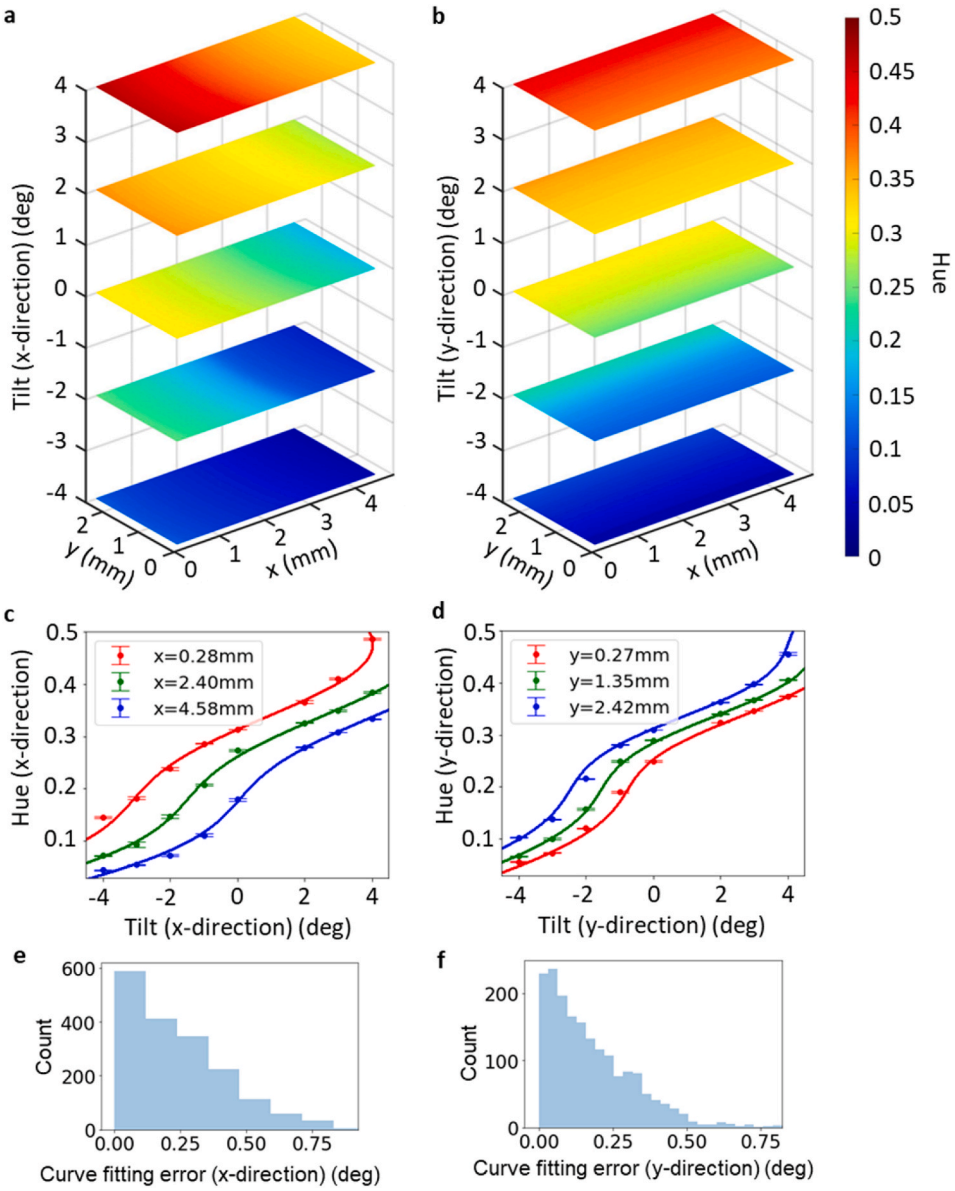

Fig. 3. Calibrating relationships between tilting angles, hue, and position using multi-dimensional curve fitting. **a**, The tilting angle in the x-direction correlated with x and y spatial positions of a micromirror and its hue value. For micromirrors of the same tilting angle, there is a gradual change of hue along the x axis, and negligible change along the y axis. We sampled experimental data at nine positions, around the edge and the center of the whole FOV on the SPOT microscopy platform. **b**, For tilting angles in the y-direction, hue value changes gradually along the y axis, and negligibly along the x axis. **c**, The relationship between the hue (x-direction) and micromirror tilting angle in the x-direction is non-linear. B-spline regression was used to optimize the curve fitting for this relationship. **d**, The relationship between the hue (y-direction) and tilting angle in the y-direction. **e**, Curve fitting error for x-direction tilting angles. Mean & median errors are 0.25 deg and 0.20 deg, respectively. **f**, Curve fitting error for y-direction tilting angles. Mean & median errors are 0.17 deg and 0.15 deg, respectively..

(Fig. 4). Details are provided in Section 6 of the Supplementary Methods. The trained model calculates the traction force distribution for a small 5 × 5 micromirror array, and therefore we fed SPOT microscopy measured tilting angle data into this model sequentially in batches (Fig. 4a). For each calculation, we select only the traction force distribution calculated near the center micromirror for subsequent processing to avoid boundary condition effects in the simulation (Fig. 4b). We filled junction areas between neighboring micromirrors using interpolation (Fig. 4c and d). We repeated this process to extract the traction force distribution on each micromirror across an entire 4.8 mm × 2.7 mm FOV (Fig. 4e).

3. Results and discussion

3.1. Traction force map

SPOT microscopy records data from the entire FOV in each frame so that post-data collection processing time and data stitching steps do not affect the measurement accuracy. This is a key difference from the conventional small FOV methods that record small-area data region by region at different times, which can introduce lag periods during data collection. For dynamic measurements, this is sub-optimal since cells' conditions may change significantly during sequential measurements. By concurrently measuring the dynamic tilting angles of all micromirrors, we can extract the dynamic traction force in every region within the whole FOV. This capability enables comparisons between traction forces at different cell sheet regions occurring at different times.

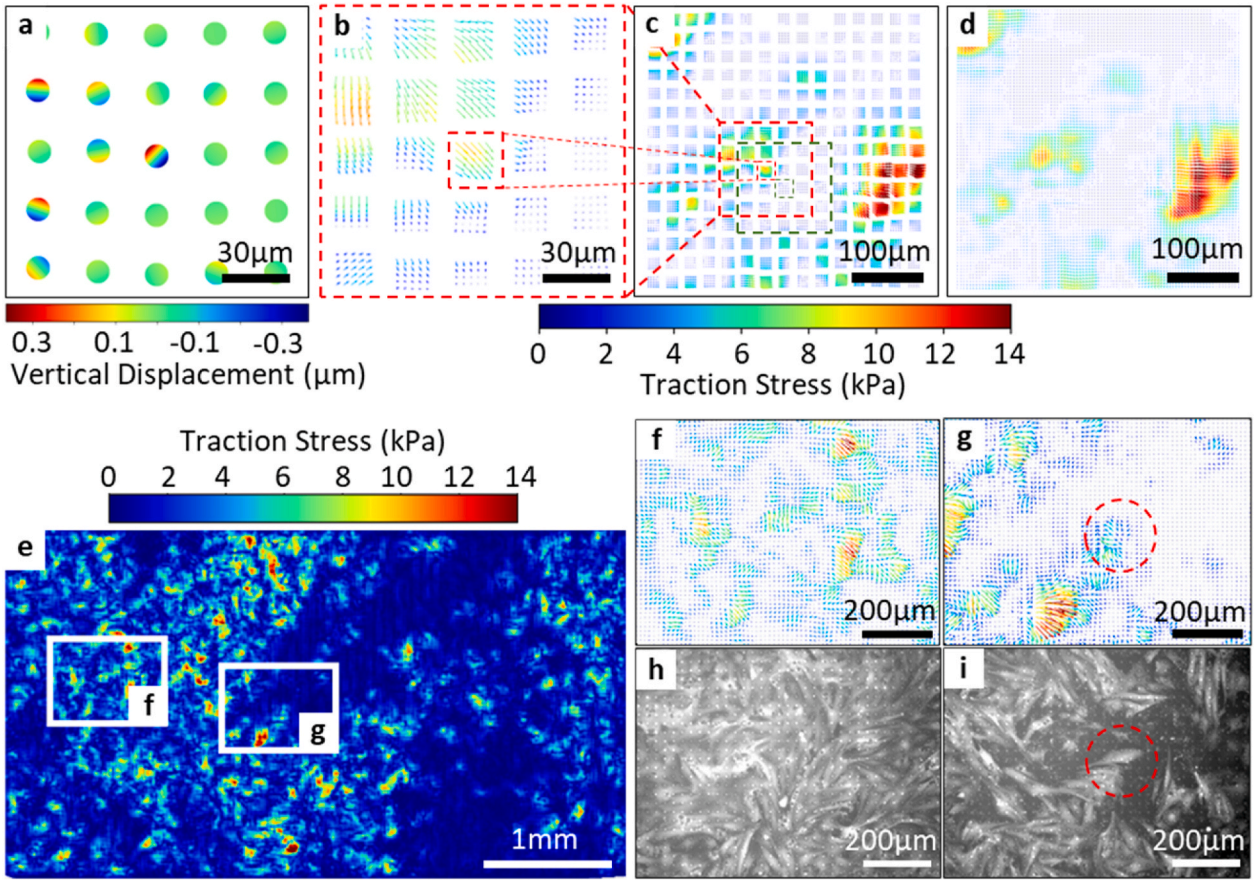

Fig. 4. Traction force distribution measurements using SPOT microscopy. a, Experimentally measured tilting angles of a 5×5 micromirror array by SPOT microscopy. **b**, A trained machine learning model computes the traction force distribution across the 5 × 5 micromirror array example in (**a**). Only the traction force distribution in the vicinity of the central micromirror is utilized for subsequent construction of larger field traction force distributions to avoid edge micromirrors that show errors due to boundary condition effects. **c,d**, Construction of the traction force distribution for the entire FOV is achieved by repeating step (**b**) and stitching through interpolation. **e,** Peak traction force distribution map of a NRVM sheet over the entire FOV. The FOV spans 4.82 mm by 2.71 mm, and the videos were taken at a frame rate of 83 frames per second. **f,g**, Peak traction force areas from selected regions in (**e**), with (**f**) showing a monolayer of NRVMs at 100% confluence, and (**g**) showing an area with a low density of NRVMs. **h**, **i,** Calcein AM fluorescent images of cells in regions corresponding to (**f**) and (**g**). The overlap between (**g**) and (**i**) at a region of nearly isolated CMs indicates that SPOT microscopy can provide sub-cellular spatial resolution of traction force distribution (see Supplementary Fig. S1).

Consequently, we can construct a map of maximum traction force distribution to quantify the beating strength of cardiomyocytes (CMs) at different regions (Fig. 4e). The cells were seeded with an overall confluence of 75%. The total area covered is 4.82 mm by 2.71 mm (Fig. 4e), which corresponds to approximately 20,000 biological cells.

We used only Neonatal Rat Ventricular Myocytes. However, the confluence of the cells at different regions within the field-of-view (Fig. 4e) vary greatly, leading to diverse configurations ranging from tightly connected tissue sheets (Fig. 4h) to clusters to near isolated cells (Fig. 4i). The collective mechanical traction stress produced differs from region to region, and from cluster to cluster. For example, there are 2 regions in Fig. 4f in which the cells push onto the substrate in the same direction, leading to regions of very high traction stresses as shown by the 2 regions with red arrows (Fig. 4f). In other regions, the cells either produce very little traction forces, or they push onto the substrate from opposite directions which lead to cancellation of traction forces. These regions are shown by the very small blue arrows (Fig. 4f). In Fig. 4g, there is a cluster near the bottom which exhibits very strong traction stresses, while clusters in other areas near the bottom right which give very weak traction stresses (Fig. 4g). Magnified images of maximum traction force distributions in selected regions are shown (Fig. 4f and g), alongside corresponding fluorescence images (Fig. 4h and i) that reveal the CM distribution. Comparing these images yields an overlap between traction force distributions and cell-occupied regions. The circled areas (Fig. 4g–i) suggest that sub-cellular spatial resolution for traction force measurements is achievable using SPOT microscopy (Supplementary Fig. S1).

3.2. Mechanical wave propagation

To demonstrate the unique capabilities of SPOT microscopy for quantifying mechanical wave propagation, we provide a sheet of beating, interconnected CMs as an experimental test bed. Efficient blood pumping depends on rhythmic, coordinated mechanical contraction and relaxation cycles to generate repeated, directional waves in a large sheet of physically interconnected CMs. In this context, we utilize SPOT microscopy to study two types of coordinated CM beating, the propagation of a typical linear plane wave and the propagation of an atypical spiral wave, which may resemble an arrhythmia clinically. Since our platform captures videos, we can extract the time-dependent variations of the pixels' intensities from the video frames. We processed the video frames by subtracting the time-averaged background frames of all the video frames. The processed video frames in Fig. 5a and b show the mechanical wave propagation. We show snapshots from a video (Fig. 5a–Supplementary Movie S1) of plane wave propagation using primary neonatal rat ventricular myocytes (NRVMs) imaged on the SPOT microscopy over a FOV of 9 mm × 9 mm. The cells were seeded with overall confluence of 75%. The total area covered is 9 mm by 9 mm

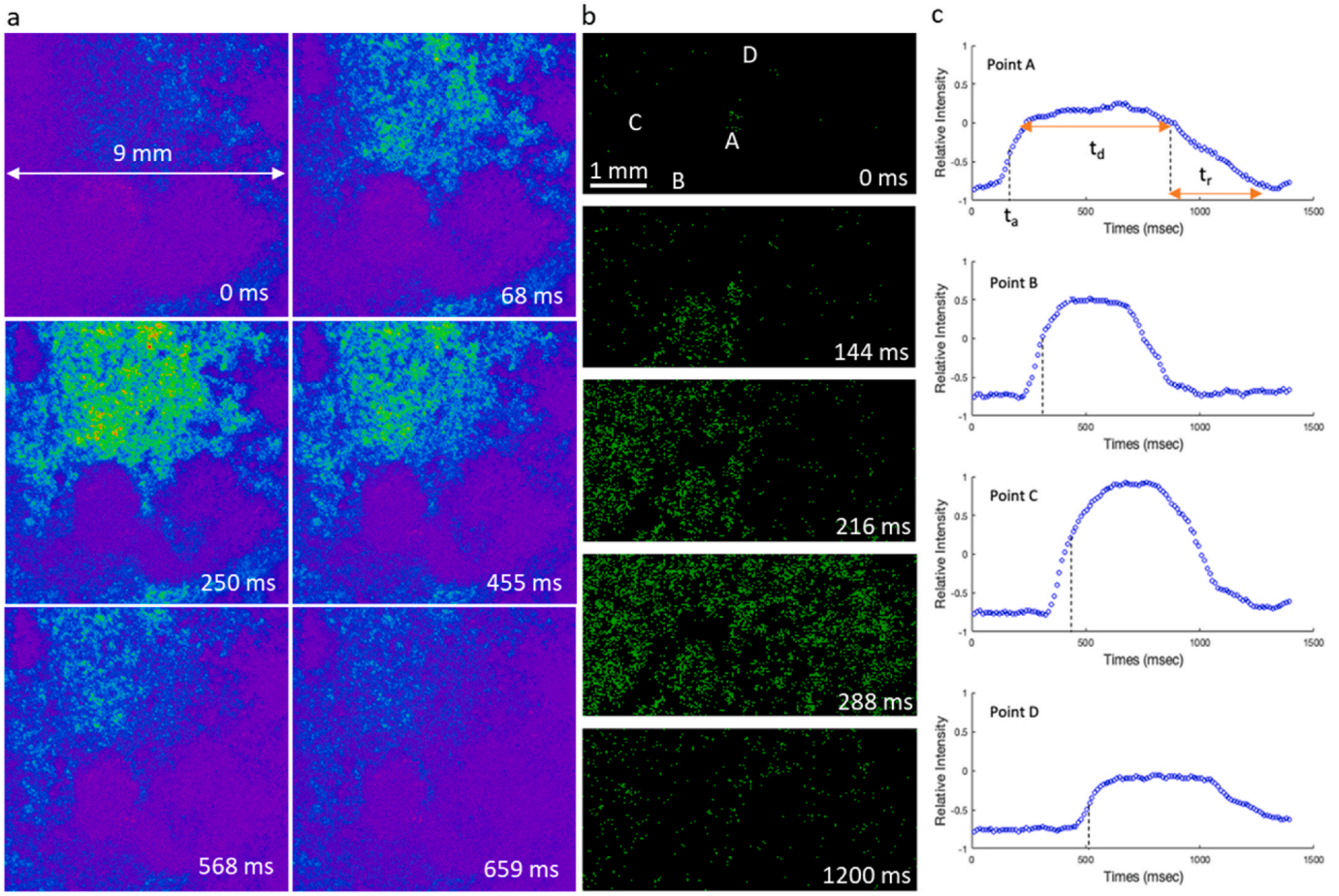

Fig. 5. SPOT microscopy captures dynamic wave propagation of beating NRVMs. a, Snapshots illustrate a plane wave propagating across a 9 mm × 9 mm field FOV (see Supplementary Movie S1). The FOV spans 9 mm by 9 mm, and the videos were taken at a frame rate of 44 frames per second. **b,** Snapshots illustrate propagation of a spiral wave initiated at the center of the FOV (see Supplementary Movie S2). The field-of-view spans 4.82 mm by 2.71 mm, and the videos were taken at a frame rate of 83 frames per second. The cells were seeded with confluence of 100%, which corresponds to approximately 26,000 biological cells. **c**, Temporal intensity profiles from selected pixels along the trajectory of a propagating spiral wave. These profiles enable the extraction of key parameters, such as activation time, contraction strength, action duration, and relaxation time, for a multi-parametric analysis of the coordinated beating behaviors of cells separated by a distance..

(Figs. 2a–5a and 6a and b), which corresponds to approximately 121,500 biological cells. The plane wave enters the FOV from the bottom right corner and gradually spreads over the entire CM sheet within 250ms. By 650ms, most of the NRVMs have completed at least one contraction and relaxation cycle. We also show snapshots from a video (Fig. 5b–Supplementary Movie S2) of a spiral wave propagation initiated at the center of the FOV that progresses in a clockwise direction. The spatiotemporal resolution of SPOT microscopy extracts dynamic intensity profiles for every pixel in the large imaging field over time. We show the time-dependent intensity profiles of four pixels along the trajectory of the mechanical spiral wave propagation (Fig. 5c). These profiles are direct measurements of forces during the contraction and relaxation cycles for individual NRVMs. SPOT microscopy can quantify multi-parametric data including activation time, contraction strength, action duration, relaxation time, beat frequency and beat pattern for each NRVM within the intercobibnnected CM sheet over time. Heterogeneities in force generation or relaxation amongst imaged CMs may uncover patterns, trends, or relationships between individual cells, subgroups of cells, and their synergistic or antagonistic activities over large areas of measurement.

3.3. Activation time maps

Application of SPOT microscopy enables the construction of an activation time map that traditionally requires OM methods to identify cells with abnormal beating rhythms. OM methods utilize fluorescent signals emitted by voltage sensitive dyes to create an activation time map. The map yields a 2D visual representation of the electrical activation sequence in cardiac tissue that uncovers the initiation, propagation and coordination of electrical signals governing the contraction and relaxation of CMs. By displaying the temporal and spatial distribution of these electrical activities, an activation time map reveals information about CM function and potential abnormalities, although different degrees of electromechanical uncoupling may yield an inaccurate representation of force generation.

In SPOT microscopy, where fluorescent signals and their experimental limitations are absent, the activation time is defined as the moment when the rate of change in the micromirror-reflected color intensity reaches its maximum. By plotting dynamic pixel intensity variations over time, we extract the activation time of each pixel from its temporal intensity profile (Supplementary Fig. S3). We provide the activation time map (Fig. 6a) corresponding to the plane wave propagation (Fig. 5a). This map identified heterogeneous cell groups with abnormal beating patterns and rhythms. We provide a map showing the relative contraction strength of NRVMs in different geographic regions of the CM sheet (Fig. 6b). By comparing maps of activation time and contraction strength, subgroups of cells showing distinctive contraction patterns and distributions can be identified using SPOT microscopy.

For an atypical spiral propagation wave, SPOT microscopy can identify the spatiotemporal origin of abnormal beating from a small

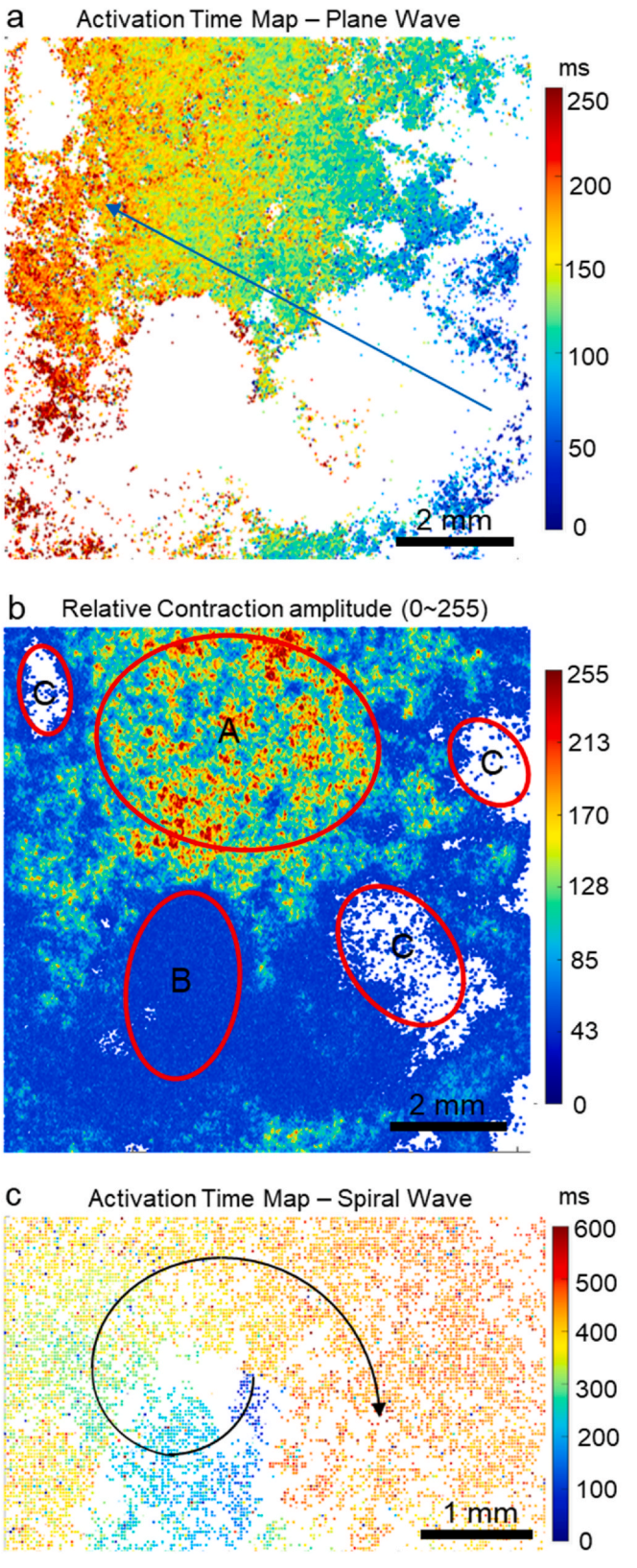

(caption on next column)

Fig. 6. SPOT microscopy captures the heterogeneity of beating cardiomyocytes (CMs). a, An activation time map corresponding to the propagating plane wave in Fig. 3a. White regions represent mostly CMs with contraction amplitude below threshold and CMs whose time-domain beating data do not fit well with the logistic fitting function used for extracting the activation time (see Fig. S4). The field-of-view spans 9 mm by 9 mm, and the videos were taken at a frame rate of 44 frames per second. **b,** A map of contraction amplitude indicates regions of distinct contraction strengths. CMs in region A show maximum contraction strength and their temporal beating patterns fit well with the logistic function used for constructing the activation time map shown in (**a**). CMs in regions B and C are groups that have contraction amplitudes lower than the threshold and were not presented in the activation time map. Yet, on the contraction amplitude plot, these two CM subgroups are clearly identified. From the bright field microscopy observation, cells in group B form a continuous sheet but have much weaker contraction strength compared to cells in group A. In contrast, C labeled regions are areas with no CMs. The field-of-view spans 9 mm by 9 mm, and the videos were taken at a frame rate of 44 frames per second. **c**, An activation time map corresponding to the propagating spiral wave shown in Fig. 3b. The spatiotemporal origin of the abnormal spiral mechanical wave can be clearly identified in this map as the deep blue cells at the base of the spiral arrow. The field-of-view spans 4.82 mm by 2.71 mm, and the videos were taken at a frame rate of 83 frames per second. The cells were seeded with confluence of 100%, which corresponds to approximately 26,000 biological cells..

cluster of CMs within the NRVM sheet (Fig. 6c), with potential implications for clinical translation. Cardiac arrhythmias can result from abnormal electrical spiral waves (Shiba et al., 2016) and SPOT microscopy reveals the mechanical manifestation of this abnormal electrical activity, which connects anomalous mechanical wave propagation to irregular CM electrical excitation.

3.4. Applications

SPOT is a general stress and strain sensing platform. As long as the sample above the SPOT platform go through certain mechanical property changes, the SPOT platform can be tailored to measure such changes. For example, an additional magnetic layer can be integrated into the SPOT micromirror array. This new magnetic SPOT platform can allow to probe the local stiffness changes the biological samples above.

In addition, since mechanical forces are important factors influencing a multiplicity of biological functions, our SPOT tool and videography platform can be used to study these cellular processes such as cytokinesis (Burton and Taylor, 1997), vaso-regulation (Hall et al., 2014), phagocytosis (Evans et al., 1993), differentiation (Lee et al., 2011), and motility (Bastounis et al., 2014). Many human illnesses are also associated with unusually strong or weak cellular traction forces. Our SPOT tool and videography platform can be used to study diseases such as cancer malignancy (Li et al., 2017), asthma (Luo et al., 2019), urological disorders (Chen et al., 2010), and cardiomyopathy (Clippinger et al., 2019).

Moreover, sub-cellular traction forces are an important bio-marker for analyzing the quality of human stem-cell derived differentiated cells in the field of regenerative medicine (Karbassi et al., 2020). In the field of heart regeneration, it is imperative that the cell traction forces of induced pluripotent stem cell (iPSC) derived cardiomyocytes be measured and checked for arrythmia in pre-clinical trials before starting any human clinical trials (Shiba et al., 2016). Furthermore, spiral cardiac waves are known to cause arrhythmias (Bingen et al., 2014). The ability of our platform to detect the shape and propagation direction of the mechanical waves is valuable in evaluating the quality of the cardiomyocyte tissue.

Currently, there is no such platform and method that can quantify these important properties to enable biologists to have comprehensive understanding of the processes occurring from the cellular level to the tissue level.

3.5. Limitations

There are a few limitations of the current SPOT platform that can be further improved in the future development. Firstly, the heat sinks used in our prototype were slow in dissipating the intense heat generated by our LEDs. Thus, continuous video recording for longer than 10 s is not supported, and the LEDs need to cool down before more recording. This can be overcome in the future by improving the heat sinks' efficiency and capacity. Secondly, the current optical grating used in the micromirrors has a linewidth of 600 nm and a periodicity of 1200 nm. This periodicity is still too large to generate sufficient spread of colors in the 1^{st} diffraction order to cover the tilting angle range of -4 to $+4$ degrees of our disks. Thus, we had to use the 2^{nd} diffraction order, which has much lower diffraction efficiency than the 1^{st} diffraction order. In the future design, if the periodicity of grating can be reduced by 2X, SPOT can utilize the 1^{st} order band with higher diffraction efficiency to lower the power requirement of LEDs and ease the challenge of heat management for long-term and continuously monitoring.

4. Conclusion

We developed a new label-free optical microscopy system to quantify rapid and dynamic mechanical wave propagation across nearly a centimeter-sized sheet of interconnected cells. Our system offers significant advantages over other indirect small FOV or fluorescence labeled approaches that suffer from potential effects on cell viability or function during measurements and limited durations of cell monitoring. In contrast, SPOT microscopy directly measures the mechanical output of cells, eliminating indirect measurements that may be variably uncoupled, and avoiding imaging-related toxicity to allow for continuous monitoring over extended periods. SPOT microscopy simultaneously records the direction and magnitude of traction forces for more than 10,000 cells, providing data with high spatiotemporal resolution. These unique multi-cellular capabilities of SPOT microscopy pave the way for a new approach and powerful platform for studies of electromechanical coupling or decoupling in CMs, arrhythmias, and drug screening, with potential for fundamental insights and ex-vivo translational applications.

CRediT authorship contribution statement

Xing Haw Marvin Tan: Writing – original draft, Visualization, Validation, Software, Resources, Methodology, Investigation, Formal analysis, Data curation, Conceptualization. **Yijie Wang:** Resources, Methodology, Investigation. **Xiongfeng Zhu:** Methodology. **Felipe Nanni Mendes:** Resources. **Pei-Shan Chung:** Methodology. **Yu Ting Chow:** Resources. **Tianxing Man:** Resources. **Hsin Lan:** Resources. **Yen-Ju Lin:** Resources. **Xiang Zhang:** Resources. **Xiaohe Zhang:** Software. **Thang Nguyen:** Resources. **Reza Ardehali:** Resources. **Michael A. Teitell:** Writing – review & editing, Supervision. **Arjun Deb:** Writing – review & editing, Supervision, Resources. **Pei-Yu Chiou:** Writing – review & editing, Visualization, Validation, Supervision, Resources, Project administration, Methodology, Funding acquisition, Formal analysis, Data curation, Conceptualization.

Declaration of competing interest

The authors declare that they have no known competing financial interests or personal relationships that could have appeared to influence the work reported in this paper.

Data availability

Data will be made available on request.

Acknowledgements

This work was supported by the National Institutes of Health grant R01GM127985; National Science Foundation grant CMMI 2029454; Department of Defense grant W81XWH2110139; A*STAR National Science Scholarship (PhD); and A*STAR Scholars' Development Fund (SDF). All fabrication steps were completed using equipment provided by the UCLA Nanoelectronics Research Facility.

Appendix A. Supplementary material

Supplementary data associated with this article can be found in the online version.

Appendix B. Supplementary data

Supplementary data to this article can be found online at https://doi.org/10.1016/j.bios.2024.116318.

References

Al-Nayili, A., Alhaidry, W.A., 2023. Res. Chem. Intermed. 49, 4239–4255.
Bao, G., Kamm, R.D., Thomas, W., Hwang, W., Fletcher, D.A., Grodzinsky, A.J., Zhu, C., Mofrad, M.R.K., 2010. Cell. Mol. Bioeng. 3, 91–105.
Bastounis, E., Meili, R., Álvarez-González, B., Francois, J., del Álamo, J.C., Firtel, R.A., Lasheras, J.C., 2014. J. Cell Biol. 204, 1045–1061.
Biggs, L.C., Kim, C.S., Miroshnikova, Y.A., Wickström, S.A., 2020. J. Invest. Dermatol. 140, 284–290.
Bingen, B.O., Engels, M.C., Schalij, M.J., Jangsangthong, W., Neshati, Z., Feola, I., Ypey, D.L., Askar, S.F.A., Panfilov, A.V., Pijnappels, D.A., de Vries, A.A.F., 2014. Cardiovasc. Res. 104, 194–205.
Burton, K., Taylor, D.L., 1997. Nature 385, 450–454.
Cameron, M., Kékesi, O., Morley, J.W., Tapson, J., Breen, P.P., van Schaik, A., Buskila, Y., 2016. PLoS One 11, e0155468.
Cansız, B., Dal, H., Kaliske, M., 2018. Comput. Mech. 62, 253–271.
Chen, C., Krishnan, R., Zhou, E., Ramachandran, A., Tambe, D., Rajendran, K., Adam, R. M., Deng, L., Fredberg, J.J., 2010. PLoS One 5, e12035.
Clippinger, S.R., Cloonan, P.E., Greenberg, L., Ernst, M., Stump, W.T., Greenberg, M.J., 2019. Proc. Natl. Acad. Sci. USA 116, 17831–17840.
Cross, S.E., Jin, Y.-S., Rao, J., Gimzewski, J.K., 2007. Nat. Nanotechnol. 2, 780–783.
Dasbiswas, K., Hu, S., Schnorrer, F., Safran, S.A., Bershadsky, A.D., 2018. Philosophical Transactions Royal Soc. B. Biol. Sci. 373, 20170114.
Dean, D.A., Ramanathan, T., Machado, D., Sundararajan, R., 2008. J. Electrost. 66, 165–177.
Ellefsen, K.L., Holt, J.R., Chang, A.C., Nourse, J.L., Arulmoli, J., Mekhdjian, A.H., Abuwarda, H., Tombola, F., Flanagan, L.A., Dunn, A.R., Parker, I., Pathak, M.M., 2019. Commun. Biol. 2, 298.
Evans, E., Leung, A., Zhelev, D., 1993. J. Cell Biol. 122, 1295–1300.
Fu, J., Wang, Y.-K., Yang, M.T., Desai, R.A., Yu, X., Liu, Z., Chen, C.S., 2010. Nat. Methods 7, 733–736.
Grosberg, A., Alford, P.W., McCain, M.L., Parker, K.K., 2011. Lab Chip 11, 4165.
Hall, C.N., Reynell, C., Gesslein, B., Hamilton, N.B., Mishra, A., Sutherland, B.A., O'Farrell, F.M., Buchan, A.M., Lauritzen, M., Attwell, D., 2014. Nature 508, 55–60.
Hardij, J., Cecchet, F., Berquand, A., Gheldof, D., Chatelain, C., Mullier, F., Chatelain, B., Dogné, J., 2013. J. Extracell. Vesicles 2.
James, B.D., Allen, J.B., 2018. ACS Biomater. Sci. Eng. 4, 3818–3842.
Kappadan, V., Telele, S., Uzelac, I., Fenton, F., Parlitz, U., Luther, S., Christoph, J., 2020. Front. Physiol. 11.
Karbassi, E., Fenix, A., Marchiano, S., Muraoka, N., Nakamura, K., Yang, X., Murry, C.E., 2020. Nat. Rev. Cardiol. 17, 341–359.
Ladoux, B., Mège, R.-M., 2017. Nat. Rev. Mol. Cell Biol. 18, 743–757.
Lapp, H., Bruegmann, T., Malan, D., Friedrichs, S., Kilgus, C., Heidsieck, A., Sasse, P., 2017. Sci. Rep. 7, 9629.
Lee, D.A., Knight, M.M., Campbell, J.J., Bader, D.L., 2011. J. Cell. Biochem. 112, 1–9.
Li, M., Dang, D., Liu, L., Xi, N., Wang, Y., 2017. IEEE Trans. NanoBioscience 16, 523–540.
Luo, M., Ni, K., Yu, P., Jin, Y., Liu, L., Li, J., Pan, Y., Deng, L., 2019. Mol. Cell. BioMech. 16, 141–151.
Matonia, A., Jezewski, J., Kupka, T., Jezewski, M., Horoba, K., Wrobel, J., Czabanski, R., Kahankowa, R., 2020. Sci. Data 7, 200.
McPheeters, M.T., Wang, Y.T., Werdich, A.A., Jenkins, M.W., Laurita, K.R., 2017. PLoS One 12, e0183761.
Pocaterra, A., Santinon, G., Romani, P., Brian, I., Dimitracopoulos, A., Ghisleni, A., Carnicer-Lombarte, A., Forcato, M., Braghetta, P., Montagner, M., Galuppini, F., Aragona, M., Pennelli, G., Bicciato, S., Gauthier, N., Franze, K., Dupont, S., 2019. J. Hepatol. 71, 130–142.
Pushkarsky, I., Tseng, P., Black, D., France, B., Warfe, L., Koziol-White, C.J., Jester, W.F., Trinh, R.K., Lin, J., Scumpia, P.O., Morrison, S.L., Panettieri, R.A., Damoiseaux, R., Di Carlo, D., 2018. Nat. Biomed. Eng. 2, 124–137.
Rodriguez, M.L., McGarry, P.J., Sniadecki, N.J., 2013. Appl. Mech. Rev. 65.
Sabass, B., Gardel, M.L., Waterman, C.M., Schwarz, U.S., 2008. Biophys. J. 94, 207–220.

Saez, A., Anon, E., Ghibaudo, M., du Roure, O., Di Meglio, J.M., Hersen, P., Silberzan, P., Buguin, A., Ladoux, B., 2010. J. Phys. Condens. Matter 22, 194119.
Sensoy, I., 2021. Curr. Res. Food Sci. 4, 308–319.
Shiba, Y., Gomibuchi, T., Seto, T., Wada, Y., Ichimura, H., Tanaka, Y., Ogasawara, T., Okada, K., Shiba, N., Sakamoto, K., Ido, D., Shiina, T., Ohkura, M., Nakai, J., Uno, N., Kazuki, Y., Oshimura, M., Minami, I., Ikeda, U., 2016. Nature 538, 388–391.
Tsukamoto, S., Fujii, T., Oyama, K., Shintani, S.A., Shimozawa, T., Kobirumaki-Shimozawa, F., Ishiwata, S., Fukuda, N., 2016. J. Gen. Physiol. 148, 341–355.
Vorselen, D., Wang, Y., de Jesus, M.M., Shah, P.K., Footer, M.J., Huse, M., Cai, W., Theriot, J.A., 2020. Nat. Commun. 11, 20.
Xiao, F., Wen, X., Tan, X.H.M., Chiou, P.-Y., 2018. Appl. Phys. Lett. 112.
Yokota, T., McCourt, J., Ma, F., Ren, S., Li, S., Kim, T.-H., Kurmangaliyev, Y.Z., Nasiri, R., Ahadian, S., Nguyen, T., Tan, X.H.M., Zhou, Y., Wu, R., Rodriguez, A., Cohn, W., Wang, Y., Whitelegge, J., Ryazantsev, S., Khademhosseini, A., Teitell, M.A., Chiou, P.-Y., Birk, D.E., Rowat, A.C., Crosbie, R.H., Pellegrini, M., Seldin, M., Lusis, A.J., Deb, A., 2020. Cell 182, 545–562.e23.
Zancla, A., Mozetic, P., Orsini, M., Forte, G., Rainer, A., 2022. J. Biol. Chem. 298, 101867.
Zhu, X., Man, T., Tan, X.H., Chung, P.-S., Teitell, M.A., Chiou, P.-Y., 2021. Lab Chip 21, 942–950.